

Escaping local minima with quantum circuit coherent cooling

Jia-Jin Feng (冯嘉进) ^{1,2} and Biao Wu (吴飙) ^{1,3,4,*}

¹International Center for Quantum Materials, School of Physics, Peking University, Beijing 100871, China

²Ming Hsieh Department of Electrical and Computer Engineering, University of Southern California, Los Angeles, California 90089, USA

³Wilczek Quantum Center, School of Physics and Astronomy, Shanghai Jiao Tong University, Shanghai 200240, China

⁴Collaborative Innovation Center of Quantum Matter, Beijing 100871, China



(Received 14 March 2023; revised 26 December 2023; accepted 9 February 2024; published 4 March 2024)

Quantum cooling has demonstrated its potential in quantum computing, which can reduce the number of control channels needed for external signals. Recent progress also supports the possibility of maintaining quantum coherence in large-scale systems. The limitations of classical algorithms trapped in the local minima of cost functions could be overcome using this scheme. According to this, we propose a hybrid quantum-classical algorithm for finding the global minima. Our approach utilizes quantum coherent cooling to facilitate coordinative tunneling through energy barriers if the classical algorithm gets stuck. The encoded Hamiltonian system represents the cost function, and a quantum coherent bath in the ground state serves as a heat sink to absorb energy from the system. Our proposed scheme can be implemented in the circuit quantum electrodynamics system using a quantum cavity. The provided numerical evidence demonstrates the quantum advantage in solving spin-glass problems.

DOI: [10.1103/PhysRevA.109.032405](https://doi.org/10.1103/PhysRevA.109.032405)

I. INTRODUCTION

Optimization problems are prevalent in many areas, where the global minima of cost functions represent the optimal solutions. Classical algorithms are usually able to quickly identify local minima but get trapped due to the complexity of the cost function. As a result, they are inefficient at finding the global minima. This bottleneck is widely recognized in various fields, including computational physics and machine learning.

We propose a hybrid quantum-classical algorithm to address this bottleneck. The entire algorithm functions as a heterogeneous cooling process to minimize the value of the cost function that encodes the given problem. The classical optimization is employed to find local minima, while the quantum cooling helps to escape the local minima by tunneling through energy barriers [1]. By alternating between classical optimization and quantum cooling, one can ultimately reach the global minimum. (See Fig. 1 for a visualization of this process.)

In the classical part of the algorithm, well-established classical techniques, such as Monte Carlo or gradient descent, are used to identify a local minimum of the cost function with minor computational resources. In the quantum part of the algorithm, the quantum icebox algorithm (QIA) performs the quantum cooling, which has been shown to achieve quantum advantage in the unsorted search problem [2]. The framework of the QIA is as follows. The cost function is encoded in a Hamiltonian system [3,4], which is initialized in the state corresponding to the local minimum. A quantum bath has a trivial and easy-to-prepare ground state that is initialized

within it. The system and the bath are coupled and maintain coherence, which facilitates coordinative quantum tunneling over high-energy barriers. The system will evolve to escape the local minimum and transition to a lower value. These two parts are complementary in order to prevent the algorithm from getting stuck.

Other hybrid quantum-classical algorithms [5–15] also combine classical and quantum methods as a compromise in the noisy intermediate-scale quantum (NISQ) era [16,17], such as the variational quantum algorithm (VQA). In the VQA, classical algorithms optimize the quantum gate parameters to reduce the number of quantum operations during the coherence time [18]. However, this approach faces challenges such as the barren plateau [9,19] and the need to avoid local minima. In our scheme, the classical algorithm only needs to optimize the initial state and find local minima, which is less problematic. Furthermore, control channels are not required during the QIA, which helps to minimize noise from external sources.

II. HETEROGENEOUS COOLING ALGORITHM

We specifically target a category of problems where the cost function involves n Boolean variables [20,21], such as the Boolean satisfiability problem and independent sets [22,23]. In physical terms, these cost functions represent Hamiltonians of (pseudo)spins [24,25]. The configuration space for these problems consists of binary strings of zeros and ones (or ± 1 for spins), with each string representing a state ψ_s . Local minima for this class of problems are defined as states where neighboring states within one Hamming distance have higher cost function values (or energies). The Hamming distance is calculated by counting the number of different bits between two binary strings [26]. To solve these problems, our

*wubiao@pku.edu.cn

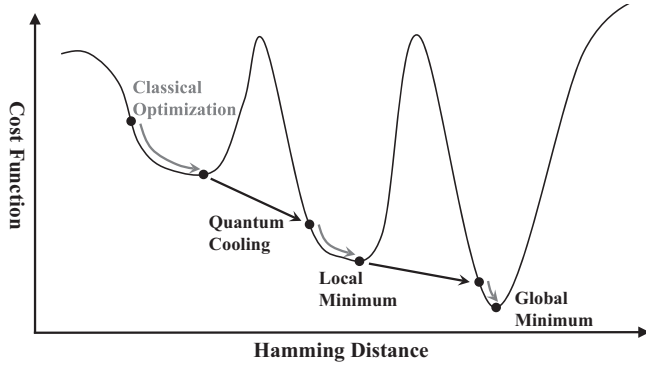


FIG. 1. Proposed heterogeneous cooling process.

hybrid quantum-classical algorithm operates as follows (see also Fig. 1).

(1) Use arbitrary configuration ψ_{s0} as the initial condition to find out one of the local minima ψ_{s1} with classical algorithms.

(2) Prepare the quantum state ψ_{s1} in the computational basis, denoted by $|\psi_{s1}\rangle$, and execute the QIA. Following quantum evolution, we obtain an entangled state $|\Psi\rangle$. We then proceed to measure the problem system in the computational basis, resulting in the random selection of a configuration denoted by ψ_{s2} .

(3) Use the configuration ψ_{s2} as the initial condition to identify a different local minimum, represented by ψ_{s3} , using classical algorithms.

(4) If $\langle \psi_{s3} | H_s | \psi_{s3} \rangle \leq \langle \psi_{s1} | H_s | \psi_{s1} \rangle$, then we update the initial configuration from ψ_{s1} to ψ_{s3} . In any case, we repeat the process starting from step 2.

(5) Stop the iteration if $\langle \psi_{s1} | H_s | \psi_{s1} \rangle$ is sufficiently small and no further update to ψ_{s1} is available.

This hybrid quantum-classical algorithm is robust to noise and errors. The long Hamming distance tunneling is divided into several shorter Hamming distance tunnelings among local minima, making it suitable for qubits with limited coherence time. Furthermore, it can identify errors in step 4 and correct them through multiple rounds of optimization. These properties make it feasible to apply them practically and implement them experimentally.

With the assistance of classical algorithms, it can efficiently reduce local energy. This hybrid algorithm achieves quantum acceleration in step 2 by utilizing the quantum bath for efficient global cooling. We can also implement continuous quantum error correction [27,28] or insert discrete quantum error correction [29,30] in step 2 to suppress errors. We will demonstrate that using the quantum bath leads to higher cooling efficiency.

III. COHERENT COOLING WITH CAVITY

Since classical algorithms are well established, let us now focus on the quantum component. We will compare the cooling efficiency of the quantum coherence bath with that of the classical bath to demonstrate the quantum advantage, particularly in the context of spin glasses. Spin glasses are typically challenging to cool down because they often have numerous local minima. Our numerical calculations demonstrate that

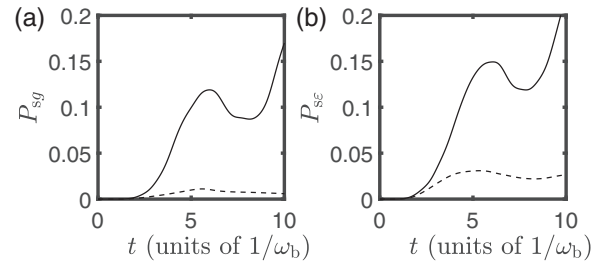


FIG. 2. Time evolution of the system cooled by the quantum bath (solid line) or the classical bath (dashed line). The number of qubits is $n_s = 11$ ($2^{-n_s} = 4.9 \times 10^{-4}$). The interaction strength is $\lambda = 0.2\hbar\omega_b$. The initial state of the problem system is the high-energy local minimum. (a) Probability of the ground state of the problem system (global minimum). (b) Total probability of states of the problem system with lower on-site energy than the initial state.

the quantum coherence bath has a faster cooling speed and a higher success rate in comparison to the classical bath (see Fig. 2).

To achieve cooling, ancilla interacting qubits are commonly used as the quantum bath [2,31–33]. However, this approach often requires at least twice the number of qubits [2,31], and maintaining entanglement among a large number of qubits is difficult in the NISQ era [16,17]. As an alternative, we use a coherent cavity as the quantum bath, which is more feasible than using hundreds of qubits. The cavity is typically used in experiments to propagate interactions [34,35] or measure states [36] and can take the form of a laser cavity [37,38], inductor-capacitor (LC) oscillator [36], or nanomechanical resonator [39].

Our discussion focuses on the circuit quantum electrodynamics systems [36], although our algorithm can also be applied to other systems. The basic setup is depicted in Fig. 3, where the cavity in the superconductor circuit can be modeled as an LC oscillator. The angular frequency of the oscillator is given by $\omega_b = 1/\sqrt{LC}$, where L is the inductance and C is the capacitance. The quantum cavity acts as the bath and its Hamiltonian is

$$H_b = \hbar\omega_b(\hat{b}^\dagger\hat{b} + \frac{1}{2}), \quad (1)$$

where \hat{b}^\dagger is the creator of the harmonic mode of the bath.

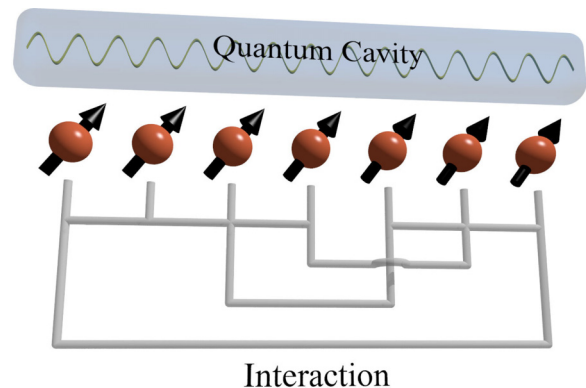


FIG. 3. Setup of our system. The coupled qubits encode the cost function and the quantum cavity serves as the bath.

The qubits in Josephson junctions store the problem data, and their interactions are established through circuit connections. The Hamiltonian encoding the problem of n_s qubits is given by [40–44]

$$H_s = \sum_{m=0}^{n_s-1} J_m^{(1)} \hat{\sigma}_m^z + \sum_{\langle m, m' \rangle} J_{m, m'}^{(2)} \hat{\sigma}_m^z \hat{\sigma}_{m'}^z, \quad (2)$$

which describes a spin glass that is difficult to cool down. The on-site energy is denoted by $J_m^{(1)}$, while $J_{m, m'}^{(2)}$ represents the interaction between two qubits. This interaction can be spatially nonlocal, making the optimization problem more challenging. To facilitate quantum transitions, $J_m^{(1)}$ and $J_{m, m'}^{(2)}$ are multiples of $\omega_b/2$. The occurrence of integer multiple gaps is common when encoding discrete mathematical problems, including nondeterministic polynomial problems [3]. It also helps to suppress overflow errors caused by unencoded energy levels.

The interaction between the qubits and the cavity in the lumped-element circuit without spatial dependence is given by [36,45–48]

$$H_\lambda = \lambda(\hat{b}^\dagger - \hat{b}) \sum_{m=0}^{n_s-1} (\hat{\sigma}_m^+ - \hat{\sigma}_m^-), \quad (3)$$

where λ is the interaction strength proportional to the capacitance. The interconnected capacitor introduces additional on-site capacitance, which can be absorbed in the parameters of H_s and H_b . Our scheme involves that $\langle H_\lambda \rangle$ is comparable to $\langle H_s \rangle$, resulting in acceleration and novel phenomena beyond the perturbation approach, including the rotating-wave approximation [49–51].

The cooling process is governed by the fixed total Hamiltonian $H = H_s + H_b + H_\lambda$ with little additional control. The circuit diagram is available in Appendix A. The total parity conservation $\exp[i\pi(b^\dagger b + 0.5 \sum_{m=0}^{n_s-1} \hat{\sigma}_m^z)]$ can slightly simplify the numerical simulation.

The initial state of the bath is its ground state [52,53], and the initial state of the problem system is set to be one of the high-energy local minima of H_s in the σ_z basis. Subsequently, the interaction H_λ is turned on and the state evolves according to the Schrödinger equation. The energy of the system is absorbed by the bath through quantum tunneling, leading to the transfer of the system's state to other local minima with lower energy.

For comparison, we treat the cavity as a classical system by defining the generalized momentum $\hat{Q}_b = i\sqrt{\hbar\omega_b C}/2(\hat{b}^\dagger - \hat{b})$ and the generalized position $\hat{\Phi}_b = \sqrt{\hbar/2\omega_b C}(\hat{b}^\dagger + \hat{b})$ [36]. If the decoherence is strong, we can treat them as classical variables Q and Φ [54–57]. The Hamiltonians for the bath in Eq. (1) and the interaction in Eq. (3) can be rewritten as

$$H_b = \frac{Q_b^2}{2C_b} + \frac{\Phi_b^2}{2L_b} \quad (4)$$

and

$$H_\lambda = \sqrt{\frac{2}{\hbar\omega_b C_b}} \lambda Q_b \sum_{m=0}^{n_s-1} \hat{\sigma}_m^y, \quad (5)$$

respectively. With the canonical equations $\partial Q_b/\partial t = \partial \langle H \rangle / \partial \Phi_b$ and $\partial \Phi_b/\partial t = \partial \langle H \rangle / \partial Q_b$ [58], we derive the total dynamical equations as

$$i\hbar \frac{\partial |\psi_s\rangle}{\partial t} = \left(H_s + \sqrt{\frac{2}{\hbar\omega_b C_b}} \lambda Q_b \sum_{m=0}^{n_s-1} \hat{\sigma}_m^y \right) |\psi_s\rangle, \quad (6)$$

$$\frac{\partial Q_b}{\partial t} = -\frac{\Phi_b}{L_b}, \quad (7)$$

$$\frac{\partial \Phi_b}{\partial t} = \frac{Q_b}{C_b} + \sqrt{\frac{2}{\hbar\omega_b C_b}} \lambda \sum_{m=0}^{n_s-1} \langle \hat{\sigma}_m^y \rangle. \quad (8)$$

Note that $Q_b = \Phi_b = 0$ is the fixed point if all the qubits are aligned in the σ_z direction. The classical bath can be treated as a classical probability ensemble. For a fair comparison, the initial state of Q_b and Φ_b is set to have the same probability distribution as the quantum ground state, which is $\rho_c = e^{-(\phi_b^2 + q_b^2)}/\pi$ with $q_b = Q_b/\sqrt{2\hbar\omega_b C_b}$ and $\phi_b = \Phi_b\sqrt{\omega_b C_b/2\hbar}$ [55,56]. The expectation value is considered as the average of all the independent evolution paths, i.e., $A = \iint a \times \rho_c dq_b d\phi_b$, where a is the observable for one initial condition and A is the expectation value.

No entanglement exists between the classical bath and the system, and the initial state of the bath ρ_c can be regarded as a mixed state. Throughout the evolution, the formation of entanglement is prohibited, and the total system remains in the product state $|\psi_s\rangle \otimes |Q, \Phi\rangle$. Moreover, some high-energy paths of the classical bath are also not allowed, even though they could help the problem system surmount barriers. The numerical results depicted in Fig. 2 demonstrate that the classical bath performs worse than its quantum counterpart.

We simulate a problem system with two local minima using Eq. (2). The initial state of the problem system is at the higher local minimum, while the bath is in its ground state. The Hamming distance between the local minima is $\lceil n_s/2 \rceil$, which increases the problem complexity. Cooling with the quantum bath does not always outperform the classical bath, but quantum resonance can strongly accelerate cooling when λ is tuned suitably [59]. Figure 2 shows the probability P_g of the ground state changing over time. Cooling with the classical bath exhibits a modest increase over time, while the curve for the quantum bath shows a sharp increase due to quantum coherent enhancement. It indicates that the QIA has an advantage in escaping local minima.

This quantum acceleration is related to the entanglement and correlation numerically calculated in Appendix B. In the continuous-variable system, we also find a similar quantum acceleration (see Appendix C).

IV. ACCELERATION BY QUANTUM WALKS EFFECT

The eigenstates of the spin-glass problem system H_s are represented by a hypercube whose vertices correspond to the eigenstates in the σ_z basis as shown in Fig. 4(a). When the interaction is turned on, the wave function diffuses in the hypercube. As depicted in Fig. 4(b), the diffusion during quantum cooling is complex with peaks at the diffusion fronts, enabling faster reaching of the answers similar to diffusion in quantum walks (QWs) [59–62]. On the other hand, the

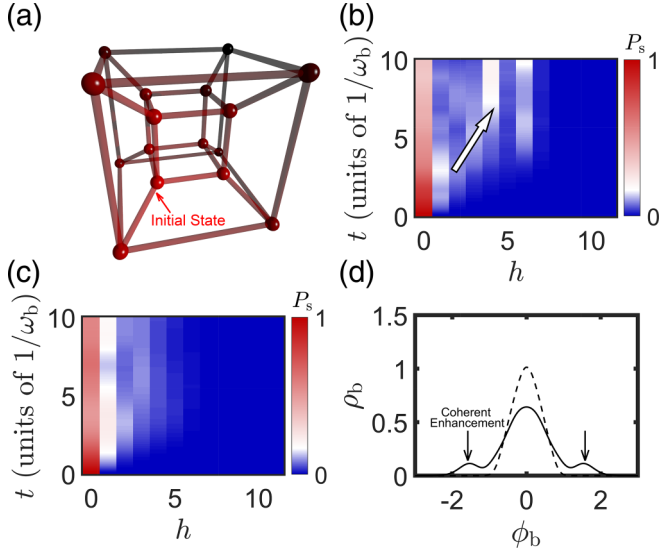


FIG. 4. (a) Hypercube where each vertex represents an eigenstate of the spin glass. The system is initially at the light red point, which is one of the local minima. The time evolution of the probability distribution is shown as the problem system is cooled by (b) the quantum bath and (c) the classical bath. Here h is the Hamming distance from the initial state; the value at each h is the addition of probabilities of different states with the same h . (d) Probability distribution of the quantum bath (solid line) and the classical bath (dashed line) at $t = 6/\omega_b$. The parameters used in the numerical computation are the same as those in Fig. 2.

diffusion during classical cooling is weaker and the probability distribution decreases monotonically with Hamming distance like the classical random walk (RW). These observations are depicted in Fig. 4(c).

Diffusion also occurs in the bath, leading to its state being driven away from its energy minimum. Better cooling performance is achieved when the bath is excited to higher-energy states with greater probability and speed. Figure 4(d) shows that the diffusion of the quantum bath is stronger with two peaks at the diffusion fronts, similar to the QW. On the other hand, the diffusion of the classical bath is weaker with monotonically decreasing fronts, as shown in Fig. 4(d). The classical bath diffuses very little without quantum coherence.

The diffusion in quantum cooling is similar to the QW, as shown by the numerical results. To further illustrate this similarity, we consider a one-qubit system with $H_s = \hbar\omega_s\hat{\sigma}_z/2$ and $\omega_s = \omega_b = \omega$. It is the Jaynes-Cummings model of nonrotating-wave form [36]. There are analytical results in the regime that one of the parameters λ , $\hbar\omega_s$, or $\hbar\omega_b$ is much smaller than the others [63]. The nonperturbative resonant regime $\lambda \sim \hbar\omega_s = \hbar\omega_b$ has rare analytical results. When the interaction is strong enough, an effective QW is observed in the dynamics. For a small time interval Δt [64], its unitary evolution is (see Appendix D for derivation)

$$U = e^{-iH\Delta t/\hbar} = e^{-iH_0\Delta t/\hbar}U_pU_H + O(\Delta t^3), \quad (9)$$

where the on-site energy is $H_0 = H_s + H_b$. For a typical Hadamard walk in a one-dimensional space with a coin qubit, its unitary operation of each iteration is $U_{QW} = U_pU_H$, where U_H is the Hadamard gate to the coin qubit and $U_p = e^{-\hat{\sigma}_z'\Delta x\partial/\partial x}$

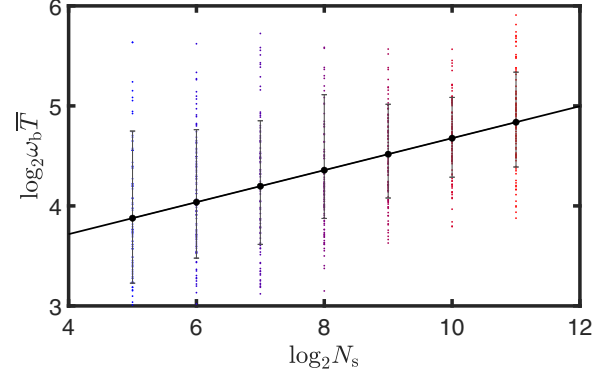


FIG. 5. Average running time \bar{T} plotted vs the size of Hilbert space N_s . Each point represents a graph in samples. The solid line represents the regression line, which has a gradient of approximately 0.16. The error bars represent the standard deviation from the regression line, primarily resulting from the fluctuation of different graphs.

is the conditional walking operator controlled by the coin qubit. Therefore, in comparison, our system has an additional punishment term $e^{-iH_0\Delta t/\hbar}$ that may disturb the phase [59]. However, this punishment term disappears when the eigenstates of H_0 involved in the evolution are degenerate. This is exactly the case that we have studied where H_s and H_b are in resonance with matching energy gaps. It is well known that the average walking distance of the RW is proportional to the square root of time $\Delta x \sim \sqrt{t}$, while that of the QW is proportional to the time $\Delta x \sim t$ [61,65]. The constructive interference makes the QW diffuse faster than the RW. It is also known that the entanglement between the coin qubit and the walking space is strong.

For the QW with multiple coin qubits, the situation is more complex (see Appendix D). The analytical results always require nonlocal operation, such as Grover's coin [66,67]. However, in our physical model, all the interactions are two-local. The numerical results in Fig. 4 suggests that the QW still contributes in this complex case.

The quantum advancement of escaping local minima can be quantitatively approach. The numerical simulation of time complexity can be seen in Fig. 5, where the size of the Hilbert space is $N_s = 2^{n_s}$. The time required for the QIA to transition between local minima is approximately $O(N_s^{0.16})$ when solving specific local interaction problems (further details in Appendix E). There are $O(n_s^{O(1)})$ energy levels for the degenerate Hamiltonian, which is proportional to the number of iterations and calls of the classical algorithm. So the total time complexity is about $O(N_s^{0.16}n_s^{O(1)})$. In addition, there are connections to each qubit, so the total space complexity is $O(n_s^2)$.

V. DISCUSSIONS

The concept of using a cavity for cooling has similarities to the quantum-circuit refrigerator (QCR) [68–70], which utilizes an open cavity to cool a system. However, the QCR exhibits strong dissipation in the cavity and some schemes utilize a dissipative qubit as the bath [71,72]. Although an open bath can introduce steady energy loss, the lack of quantum

coherence may hinder the cooling process. Recent research suggests that the non-Markovian baths could improve the performance of a quantum refrigerator [73,74]. In Appendix F we show that the dissipation in the quantum bath will slow down the cooling speed.

In conclusion, we proposed a hybrid quantum-classical algorithm of coherent cooling to address the issue of local minima. It encodes the cost function in a superconductor circuit cooled by a quantum cavity, which outperforms a classical cavity due to the coordinative tunneling effect. Our results suggest that the faster diffusion of the QW over the classical RW is the underlying physics of this quantum speedup. While we have focused on discrete-variable problems, our scheme can be extended to continuous-variable problems. This hybrid algorithm is expected to streamline the control and reduce noise in quantum computing experiments.

ACKNOWLEDGMENTS

B.W. and J.-J.F. were supported by the National Key R&D Program of China (Grants No. 2017YFA0303302 and No. 2018YFA0305602), National Natural Science Foundation of China (Grant No. 11921005), and Shanghai Municipal Science and Technology Major Project (Grant No. 2019SHZDZX01).

APPENDIX A: SUPERCONDUCTOR CIRCUIT OF COHERENT COOLING

Superconductor circuits can be utilized to physically implement the quantum icebox algorithm, and we can use the simplest charge qubits of Josephson junction as an example as shown in Fig. 6. Other types of qubits require slight modifications. For phase qubits, an additional injected current is needed for each qubit. For flux qubits, the on-site capacitors are replaced by inductors and the interconnected capacitors are replaced by mutual inductors [42,75,76]. The on-site energy $J_m^{(1)}$ can be tuned by the parallel capacitance of each qubit, while the interaction $J_{m,m'}^{(2)}$ depends on the connectivity and coupling strength of the circuit matrix. The ZZ interaction is usually achieved by effective indirect interaction [40,42,77]. If the coherence of long-distance interaction is poor, indirect interaction can be used to improve it [34,35,78–82]. The crosstalk can be suppressed by a thick insulating layer made of high dielectric constant materials [80].

The design shown in Fig. 6 is inspired by the matrix circuit, a design commonly used in classical circuits for devices like screens, keyboards, and memories. The information is encoded in the intersections of the rows and columns, and only two circuit layers are needed. IBM has already realized the multilayer chip of the quantum computer, while there are tens of layers used in modern classical CPUs.

APPENDIX B: INFLUENCE OF STRONG INTERACTION

For quantum acceleration, strong interaction is required to overcome localization, which typically occurs in low-symmetry quantum systems and suppresses the propagation of wave functions [83,84].

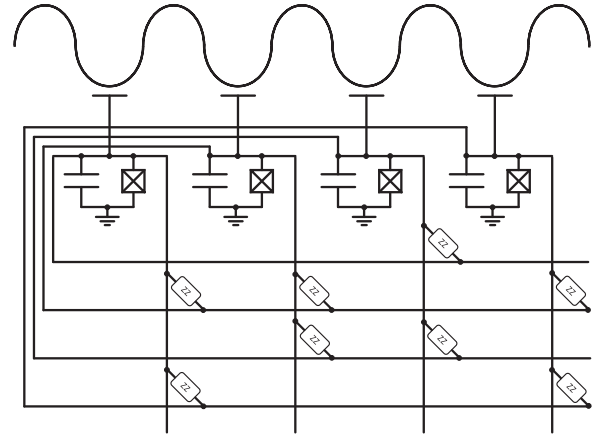


FIG. 6. Superconductor circuit of coherence cooling with the cavity. The long curve on the top is the cavity modeled by the LC oscillator. The symbol with a cross inside the square is the Josephson junction, which constitutes the qubit with the parallel capacitor. There is no connection of each intersection between wires without a dot.

We begin by examining the eigenstates of the total Hamiltonian $H = H_s + H_b + H_\lambda$. In the absence of interaction ($H_\lambda = 0$), the eigenstates are product states of the system and bath. The system is fully localized at the vertex of the hypercube in the σ_z basis, with no nearby probability distribution. If localization decreases, probability distribution appears nearby, and the peak of probability P_{\max} decreases as the probability is shared with other states. Thus, localization strength can be determined by P_{\max} of eigenstates with low energy, shown in Fig. 7(a). Weak interaction λ results in highly localized eigenstates [84], as seen on the left-hand side of Fig. 7(a), where the wave function is unable to reach the whole

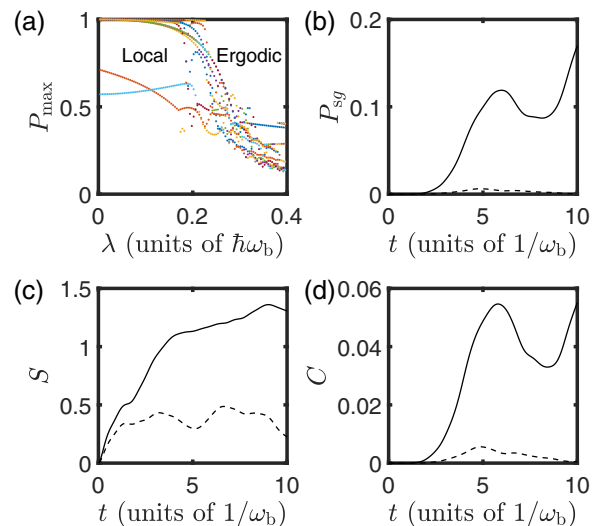


FIG. 7. (a) Localization strength of ten low-energy eigenstates distinguished by different colors. Also shown is the time-dependent evolution of (b) the ground-state probability of the problem system, (c) the entanglement entropy, and (d) the correlation of joint probability. The interaction strength is $\lambda = 0.2\hbar\omega_b$ (solid line) and $\lambda = 0.15\hbar\omega_b$ (dashed line).

Hilbert space, preventing solution discovery. On the other hand, strong interaction causes delocalization [59,85,86], as shown on the right-hand side of Fig. 7(a), with sufficient probability distribution around the ground state.

Furthermore, the degree of localization can also impact the strength of revivals. Revivals typically occur in (pseudo)integrable systems, where the state after evolution partially returns to its initial state. When the interaction is weak, only a few states are involved, resulting in strong revivals, as illustrated by the dashed line in Fig. 7(b). On the other hand, when the interaction is comparable to the on-site energy, more states are involved, leading to a rich energy spectrum of the initial state and weaker revivals, as shown by the solid line in Fig. 7(b).

We use the entanglement entropy and correlation to further investigate the quantum coherence between the quantum bath and the problem system. The entanglement entropy is given by

$$S = -\text{Tr}(\rho_s \ln \rho_s), \quad (\text{B1})$$

where $\rho_s = \text{Tr}_b(\rho)$ is the reduced density matrix of the problem system. The entanglement entropy is shown in Fig. 7(c). The correlation can be described by the joint probability defined as [87]

$$\begin{aligned} C &= \langle \hat{P}_{sg}(\hat{I} - \hat{P}_{bg}) \rangle - \langle \hat{P}_{sg} \rangle \langle \hat{I} - \hat{P}_{bg} \rangle \\ &= -\langle \hat{P}_{sg} \hat{P}_{bg} \rangle + \langle \hat{P}_{sg} \rangle \langle \hat{P}_{bg} \rangle. \end{aligned} \quad (\text{B2})$$

Figure 7(d) shows the correlation.

When the interaction between the problem system and the bath is weak $\langle H_\lambda \rangle \ll \langle H_0 \rangle$, the bath's influence can be considered a perturbation. Thus, the composed system can be approximated as a product state of the problem system and the bath, and the rotating-wave approximation (RWA) holds to a large extent. Both the entanglement entropy and correlation are small, as shown by the dashed lines in Fig. 7. In this scenario, the localization is strong, but the cooling efficiency is low [84].

As the interaction strength becomes comparable to the on-site energy $\langle H_\lambda \rangle \sim \langle H_0 \rangle$, the composed system undergoes a phase transition [88] and the wave function becomes delocalized and ergodic [85,86]. The product state approximation of the problem system and the bath is no longer valid. The entanglement and correlation between them increase significantly, as depicted by the solid lines in Fig. 7, while the entanglement between the system and the classical bath is absent.

In the extremely strong coupling regime, the interaction H_λ dominates the dynamics. Despite the strong entanglement and correlation, the information from the system with $H \approx H_\lambda$ is limited. Consequently, the cooling effect will vanish, leading to a low success rate.

APPENDIX C: COOLING THE CONTINUOUS SYSTEM

The problems associated with continuous dynamical variables can also be encoded in the Hamiltonian, for example, by mapping the variables to the generalized positions Φ_s of Josephson junctions. The cost function for such a problem can

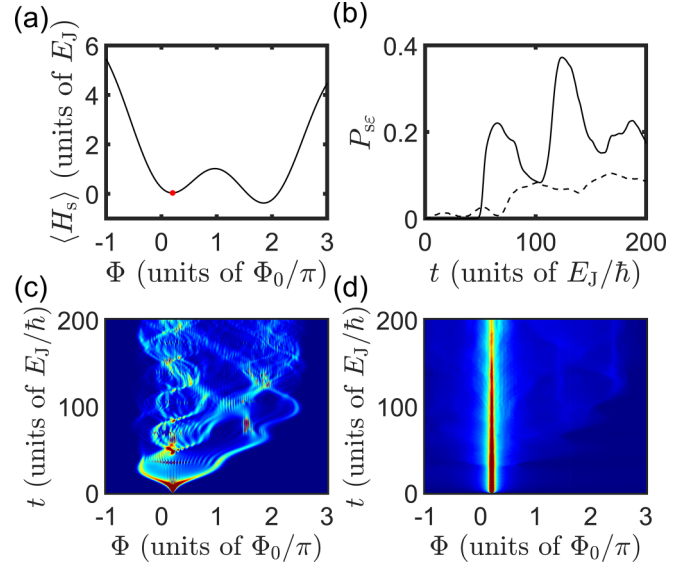


FIG. 8. (a) System energy as a function of Φ ; the red point indicates the initial state. (b) Time evolution of the total probability of the states which have lower on-site energy than the initial state. The solid line is for cooling using the quantum bath, while the dashed line is cooling using the classical bath. Also shown is the time evolution of the probability distribution of the system with (c) the quantum bath and (d) the classical bath (red for high values and blue for low).

be encoded in a Hamiltonian as

$$H_s = \frac{(\hat{\Phi}_s - \Phi_{ex})^2}{2L_s} - E_J \cos \frac{2\pi \hat{\Phi}_s}{\Phi_0}, \quad (\text{C1})$$

where Φ_{ex} is the external magnetic flux, Φ_0 is the quantum magnetic flux, L_s is the inductance, and E_J is the Josephson energy. These parameters can all be tuned [89]. The goal is to find the global minimum on Φ_s , with the shape of the cost function shown in Fig. 8(a). The initial state is set at the higher local minimum.

The system-bath interaction can arise via the capacitor connection. This interaction can be described by the Hamiltonian

$$H_\lambda = -\frac{\hat{Q}_s \hat{Q}_b}{C_\lambda}, \quad (\text{C2})$$

where C_λ is the effective capacitance of the connection. The influence of the on-site capacitance has already been included in the parameters of H_s and H_b .

The cooling process with the quantum bath satisfies the Schrödinger equation. The cooling process using the classical bath satisfies the equations

$$i\hbar \frac{\partial |\psi_s\rangle}{\partial t} = \left(H_s - \frac{Q_b}{C_\lambda} \hat{Q}_s \right) |\psi_s\rangle, \quad (\text{C3})$$

$$\frac{\partial Q_b}{\partial t} = -\frac{\Phi_b}{L_b}, \quad (\text{C4})$$

$$\frac{\partial \Phi_b}{\partial t} = \frac{Q_b}{C_b} - \frac{\langle \hat{Q}_s \rangle}{C_\lambda}. \quad (\text{C5})$$

Comparing the time evolutions in Fig. 8(b), it is observed that the quantum bath yields better cooling efficiency than the classical bath in the continuous-variable scenario. The

quantum cooling displays characteristic quantum oscillations, while classical cooling is smoother. Figure 8(c) illustrates the coherent diffusion of quantum cooling through coordinative tunneling in the position space, displaying strong coherent enhancement at the wave function's fronts. Figure 8(d) shows the smoother incoherent diffusion of classical cooling, with the strongest component trapped in the higher local minimum.

APPENDIX D: QUANTUM WALK EFFECT IN THE COHERENT COOLING

Governed by the Schrödinger equation, the time evolution of the composed Hamiltonian can be divided into small steps

$$e^{-iHt/\hbar} = \prod_{n=1}^{t/\Delta t} e^{-iH\Delta t/\hbar}. \quad (\text{D1})$$

The unitary operator for each step, $U = e^{-iH\Delta t/\hbar}$ for the Hamiltonian in Eq. (9), can be approximated as [64]

$$\begin{aligned} U &= \exp\left(-i\frac{\omega}{2}\hat{\sigma}_z\Delta t - i\omega(\hat{q}_b^2 + \hat{\phi}_b^2)\Delta t + i2\frac{\lambda}{\hbar}\hat{\sigma}_y\hat{q}_b\Delta t\right) \\ &\approx \exp\left(-i\frac{\omega}{2}\hat{\sigma}_z\Delta t - i\omega(\hat{q}_b^2 + \hat{\phi}_b^2)\Delta t\right) \exp\left(i2\frac{\lambda}{\hbar}\hat{\sigma}_y\hat{q}_b\Delta t\right) \\ &\quad \times \exp\left(-\frac{1}{2}\left[-i\frac{\omega}{2}\hat{\sigma}_z\Delta t, i2\frac{\lambda}{\hbar}\hat{\sigma}_y\hat{q}_b\Delta t\right]\right) \\ &\quad \times \exp\left(-\frac{1}{2}\left[-i\omega(\hat{q}_b^2 + \hat{\phi}_b^2)\Delta t, i2\frac{\lambda}{\hbar}\hat{\sigma}_y\hat{q}_b\Delta t\right]\right) \\ &= \exp^{-i\frac{\omega}{2}\hat{\sigma}_z\Delta t - i\omega(\hat{q}_b^2 + \hat{\phi}_b^2)\Delta t} \exp^{i2\frac{\lambda}{\hbar}\hat{\sigma}_y\hat{q}_b\Delta t} \exp^{i\frac{\lambda}{\hbar}\omega\hat{\sigma}_x\hat{q}_b\Delta t^2} \\ &\quad \times \exp^{-i\omega\frac{\lambda}{\hbar}\hat{\sigma}_y\hat{\phi}_b\Delta t^2} \\ &\approx \exp\left(-i\frac{\omega}{2}\hat{\sigma}_z\Delta t - i\omega(\hat{q}_b^2 + \hat{\phi}_b^2)\Delta t\right) \\ &\quad \times \exp\left(i\frac{\lambda}{\hbar}(2\Delta t\hat{\sigma}_y + \omega\Delta t^2\hat{\sigma}_x)\hat{q}_b\right) \\ &\quad \times \exp\left(-i\omega\frac{\lambda}{\hbar}\hat{\sigma}_y\hat{\phi}_b\Delta t^2\right), \end{aligned} \quad (\text{D2})$$

where we have omitted all the $O(\Delta t^3)$ terms. The dimensionless operator is $\hat{q}_b = -i\partial/\partial\phi_b$. Note that the angle of rotation axis between U_p and U_H of the coin qubit is $\pi/4$ in the Hadamard walk. In the time interval $\Delta t = 2/\omega$, this condition will be satisfied with

$$\begin{aligned} U &= \exp\left(-i\frac{H_0\Delta t}{\hbar}\right) \exp\left(-\frac{2\sqrt{2}\lambda}{\hbar\omega}\frac{\hat{\sigma}_y + \hat{\sigma}_x}{\sqrt{2}}\frac{\partial}{\partial\phi_b}\right) \\ &\quad \times \exp\left(-i\frac{4\lambda}{\hbar\omega}\hat{\sigma}_y\hat{\phi}_b\right). \end{aligned} \quad (\text{D3})$$

Then the rotation axis between the last two terms is also $\pi/4$. To simplify the comparison with the Hadamard walk, we make the following transformations:

$$\begin{aligned} \hat{\sigma}_z &= \hat{\sigma}'_x, \\ \hat{\sigma}_x &= \frac{\hat{\sigma}'_z - \hat{\sigma}'_x}{\sqrt{2}}, \\ \hat{\sigma}_y &= \frac{\hat{\sigma}'_z + \hat{\sigma}'_x}{\sqrt{2}}. \end{aligned} \quad (\text{D4})$$

Then the operation becomes

$$\begin{aligned} U &= \exp\left(-i\frac{H_0\Delta t}{\hbar}\right) \exp\left(-\hat{\sigma}'_z\frac{2\sqrt{2}\lambda}{\hbar\omega}\frac{\partial}{\partial\phi_b}\right) \\ &\quad \times \exp\left(i\frac{4\lambda}{\hbar\omega}\frac{\hat{\sigma}'_z + \hat{\sigma}'_x}{\sqrt{2}}\hat{\phi}_b\right). \end{aligned} \quad (\text{D5})$$

When $4\lambda\phi_b/\hbar\omega = (2n+1)\pi$, namely, $\Delta\phi_b = \pi_b\hbar\omega/2\lambda$, the last term is the Hadamard gate. Moreover, the displacement of conditional translation is $\Delta\phi_b = 2\sqrt{2}\lambda/\hbar\omega$, so self-consistency requires $\lambda = \sqrt{\pi}/2^{5/4}\hbar\omega$. In summary, the unitary operation is

$$U = \exp\left(-i\frac{H_0\Delta t}{\hbar}\right) U_p U_H. \quad (\text{D6})$$

Except for the term $\exp(-i\frac{H_0\Delta t}{\hbar})$, this is just the standard Hadamard walk.

In the case of a spin glass with multiqubits, the operation is

$$U = \exp\left(-i\frac{H_0\Delta t}{\hbar}\right) U_p U_H^{\otimes n_s}, \quad (\text{D7})$$

where the Hadamard gates require $\omega_b\lambda\Delta\phi_b\Delta t^2/\hbar = 2\pi$. The conditional walker is more complex such that

$$\begin{aligned} U_p &= \exp\left[i\frac{\lambda}{\hbar}\left(\sum_{m=1}^{n_s}\Delta t\hat{\sigma}_m^y + \sum_{m=1}^{n_s}J_m^{(1)}\Delta t^2\hat{\sigma}_m^x\right.\right. \\ &\quad \left.\left.+ \sum_{(m,m')}J_{m,m'}^{(2)}\Delta t^2(\hat{\sigma}_m^x\hat{\sigma}_{m'}^z + \hat{\sigma}_m^z\hat{\sigma}_{m'}^x)\right)\frac{\partial}{\partial\phi_b}\right]. \end{aligned} \quad (\text{D8})$$

APPENDIX E: TIME COMPLEXITY

In this Appendix we attempt to evaluate the time complexity of our algorithm. Our algorithm is general and applicable to many optimization problems. However, in order to gain informative results with limited computational resources, we need to narrow our focus to a specific set of problems. These optimization problems are constructed in the following manner. All qubits are first connected in a one-dimensional chain to make them inseparable. We then connect each qubit to another randomly selected qubit. The number of links for each qubit ranges from 2 to $n_s + 2$, with an average of $2 - 0.5/n_s$ links per qubit. Ferromagnetic interaction exists only between two connected qubits with equal strength. As a result, there are two global minima $|0\rangle^{\otimes n_s}$ and $|1\rangle^{\otimes n_s}$. Finally, we add on-site energy to certain qubits. The two ground states will split: One becomes a local minimum with high energy and the other remains a global minimum.

For a system with n_s qubits, it can correspond to a graph. As there are $O(2^{n_s^2})$ different graphs, the configuration space is extremely large. It is difficult to traverse all of the graphs. As a compromise, we sample 100 graphs following the mentioned rule for each value of n_s and consider them as typical.

If the problem system reaches the global minimum, we consider the cooling process successful, which can be described by the characteristic time τ and the success rate P_T . The characteristic time τ refers to the speed at which the dynamics reaches equilibrium. The success rate τ is the total

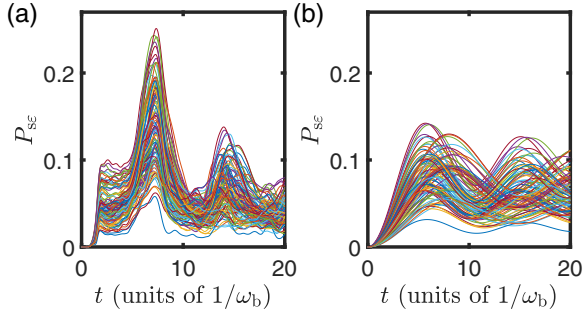


FIG. 9. (a) Time-dependent total probability of states that have lower on-site energy than the initial state. Different colors represent different graphs. The size of the problem system is $n_s = 11$. (b) Fitting curves of (a) with just two adjustable parameters.

probability at the global minimum when the dynamics reaches equilibrium. To extract the characteristic time and success rate, we fit the numerical results with the function

$$P_{se} \approx P_r f\left(\frac{t}{\tau}\right), \quad (\text{E1})$$

where the function has the properties that $\lim_{x \rightarrow +\infty} f(x) = 1$ and $\lim_{x \rightarrow 0} f(x)/x^2 = \text{const}$. Using the fitting function can suppress the poisoning of the results caused by accidental narrow peaks and outliers. Here we have chosen the fitting function to be $f(x) = 1 - J_0(x)$, where $J_0(x)$ is the zeroth-order Bessel function of the first kind. The fitting performance is shown in Fig. 9. Since there are only two free parameters, the fitting may not be perfect. Other fitting functions are tried, yielding parameters of similar magnitude.

Now we will begin analyzing the time complexity. The average running time can be defined as

$$\bar{T} = \frac{\tau}{P_r - \frac{1}{N_s}}, \quad (\text{E2})$$

where τ is the characteristic time of the dynamics and P_r is the success rate. The \bar{T} is approximately proportional to the runtime required to achieve a given success rate. If P_r is smaller, more attempts and measurements will be required. If the interaction is exceedingly strong, the system will rapidly become ergodic. However, there is no calculation associated with this type of probability increment. So we subtract the background probability of such a wild guess, which is $1/N_s = 2^{-n_s}$. The average running time against the system's size is shown in Fig. 5. The best and worst cases are not shown because they are difficult to sample with a large value of n_s . For the average case in samples, the regression yields a gradient of approximately 0.16. The time complexity for each successful cooling is $O(N_s^{0.16})$.

The encoding Hamiltonian is highly degenerate with $O(n_s^{O(1)})$ energy levels. The maximum number of iterations required to reach the lowest-energy levels is also bounded by $O(n_s^{O(1)})$. Specifically, it is $O(n_s^3)$ for solving the maximal independent set problem with the two-local Hamiltonian.

In summary, the total average time complexity is approximately $O(N_s^{0.16} \log^3 N_s) = O(1.12 n_s^3)$. The time complexity of the classical algorithm is approximately $O(1.19 n_s^{O(1)})$ [90].

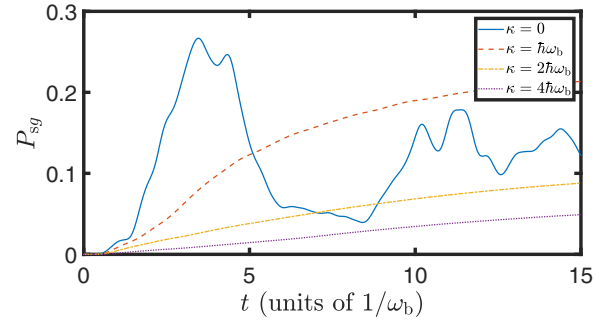


FIG. 10. Ground-state probability of the problem system with different decoherence strength κ of the bath. The other parameters are $n_s = 5$ and $\lambda = 0.6\hbar\omega_b$.

APPENDIX F: DECOHERENCE WITH THE MARKOV MASTER EQUATION

In the main text we discussed cooling with a coherent quantum bath using the Schrödinger equation. However, the experiment always faces decoherence, such as the thermal bath, which has been shown to easily reach local minima [91]. Now we investigate the ability to reach the global minimum and treat the cooling with the Markov master equation [92,93]

$$\frac{d\rho}{dt} = -\frac{i}{\hbar}[H, \rho] - \frac{\kappa}{\hbar}(b^\dagger b \rho + \rho b^\dagger b - 2b \rho b^\dagger), \quad (\text{F1})$$

where κ represents the decoherence strength of the bath. In Fig. 10 we compare the cooling processes with different values of κ . The case with $\kappa = 0$ corresponds to the case discussed in the main text.

The numerical results indicate that the cooling process without decoherence is faster in the early stage. Although decoherence can extract energy from the bath irreversibly, it can disrupt the quantum acceleration by suppressing the off-diagonal terms of the density matrix ρ . This transition between quantum states requires these off-diagonal terms, and the presence of decoherence can hinder quantum tunneling.

At the late cooling stage, the cooling process reaches saturation. Even a small amount of decoherence can decrease the revival from quantum oscillation [83,94]. Strong decoherence, on the other hand, can entirely suppress the quantum transition.

We consider a simple case to demonstrate the effect of decoherence on quantum acceleration, where both the problem system and the bath are two-level systems [73,74]. The states $|\sigma_z, n_b\rangle$ are redefined as $|2\rangle \equiv |1, 0\rangle$, $|1\rangle \equiv |-1, 1\rangle$, and $|0\rangle \equiv |-1, 0\rangle$. Equation (F1) in the RWA can then be written as

$$\frac{d\rho_{22}}{dt} = \frac{\lambda}{\hbar}(i\rho_{12} - i\rho_{21}), \quad (\text{F2})$$

$$\frac{d\rho_{12}}{dt} = \frac{\lambda}{\hbar}(i\rho_{22} - i\rho_{11}) - \frac{\kappa}{\hbar}\rho_{12}, \quad (\text{F3})$$

$$\frac{d\rho_{11}}{dt} = \frac{\lambda}{\hbar}(-i\rho_{12} + i\rho_{21}) - 2\frac{\kappa}{\hbar}\rho_{11}, \quad (\text{F4})$$

$$\frac{d\rho_{00}}{dt} = 2\frac{\kappa}{\hbar}\rho_{11}, \quad (\text{F5})$$

where $\rho_{12}^\dagger = \rho_{21}$. The initial condition is $\rho_{22} = 1$ and other elements of the density matrix are zero. The solution is

$$\rho_{22} = e^{-\kappa t/\hbar} \left(\frac{1 + \cos 2\Omega t}{2} \frac{\lambda^2}{\hbar^2 \Omega^2} - \frac{\cos 2\Omega t}{4} \frac{\kappa^2}{\hbar^2 \Omega^2} + \frac{\sin 2\Omega t}{4} \frac{\kappa}{\hbar \Omega} \right), \quad (\text{F6})$$

where $\hbar\Omega = \sqrt{\lambda^2 - \kappa^2/4}$ and $P_{sg} = 1 - \rho_{22} = \rho_{11} + \rho_{00}$. It is a damped oscillator with the decoherence κ slowing down the oscillation angular frequency from λ/\hbar to Ω . As a result, the quantum transition between $|2\rangle$ and $|1\rangle$ is also slowed down.

When the decoherence is small $\kappa \ll \lambda$, the system is in the underdamped regime with oscillations. The probability of being in the ground state is approximately given by

$$P_{sg} \approx 1 - e^{-\kappa t/\hbar} \left(\frac{1 + \cos \frac{2\lambda t}{\hbar}}{2} + \frac{\kappa}{2\lambda} \sin \frac{2\lambda t}{\hbar} \right). \quad (\text{F7})$$

In the early stage $t \ll \hbar/\lambda$, Eq. (F7) can be simplified to

$$P_{sg} \approx \sin^2 \frac{\lambda t}{\hbar} - \frac{\lambda^2 \kappa}{2\hbar^3} t^3. \quad (\text{F8})$$

The last term is due to decoherence, and its negativity implies that it leads to deceleration.

When $\kappa \gg \lambda$, the system is in the overdamped regime without oscillations and the ground state probability is given by

$$P_{sg} \approx 1 - e^{-(2\lambda^2/\hbar\kappa)t}, \quad (\text{F9})$$

which indicates that stronger decoherence leads to slower cooling. In this regime, the bath is almost frozen in its ground state and the dynamics is essentially static.

For multiqubits, as depicted in Fig. 10, there is also exponential behavior observed in the presence of strong dissipation, similar to Eq. (F9). Therefore, to ensure reasonable quantum acceleration, the decoherence strength should not greatly exceed the tunneling strength during quantum computing.

-
- [1] J. R. Espinosa, Tunneling without bounce, *Phys. Rev. D* **100**, 105002 (2019).
- [2] J.-J. Feng, B. Wu, and F. Wilczek, Quantum computing by coherent cooling, *Phys. Rev. A* **105**, 052601 (2022).
- [3] E. Farhi, J. Goldstone, S. Gutmann, J. Lapan, A. Lundgren, and D. Preda, A quantum adiabatic evolution algorithm applied to random instances of an NP-complete problem, *Science* **292**, 472 (2001).
- [4] S. Ebadi, A. Keesling, M. Cain, T. T. Wang, H. Levine, D. Bluvstein, G. Semeghini, A. Omran, J.-G. Liu, R. Samajdar, X.-Z. Luo, B. Nash, X. Gao, B. Barak, E. Farhi, S. Sachdev, N. Gemelke, L. Zhou, S. Choi, H. Pichler *et al.*, Quantum optimization of maximum independent set using Rydberg atom arrays, *Science* **376**, 1209 (2022).
- [5] E. Farhi, J. Goldstone, and S. Gutmann, A quantum approximate optimization algorithm, [arXiv:1411.4028](https://arxiv.org/abs/1411.4028).
- [6] A. Peruzzo, J. McClean, P. Shadbolt, M.-H. Yung, X.-Q. Zhou, P. J. Love, A. Aspuru-Guzik, and J. L. O'Brien, A variational eigenvalue solver on a photonic quantum processor, *Nat. Commun.* **5**, 4213 (2014).
- [7] J. R. McClean, J. Romero, R. Babbush, and A. Aspuru-Guzik, The theory of variational hybrid quantum-classical algorithms, *New J. Phys.* **18**, 023023 (2016).
- [8] J. I. Colless, V. V. Ramasesh, D. Dahlen, M. S. Blok, M. E. Kimchi-Schwartz, J. R. McClean, J. Carter, W. A. de Jong, and I. Siddiqi, Computation of molecular spectra on a quantum processor with an error-resilient algorithm, *Phys. Rev. X* **8**, 011021 (2018).
- [9] J. R. McClean, S. Boixo, V. N. Smelyanskiy, R. Babbush, and H. Neven, Barren plateaus in quantum neural network training landscapes, *Nat. Commun.* **9**, 4812 (2018).
- [10] S. McArdle, T. Jones, S. Endo, Y. Li, S. C. Benjamin, and X. Yuan, Variational ansatz-based quantum simulation of imaginary time evolution, *npj Quantum Inf.* **5**, 75 (2019).
- [11] L. Zhou, S.-T. Wang, S. Choi, H. Pichler, and M. D. Lukin, Quantum approximate optimization algorithm: Performance, mechanism, and implementation on near-term devices, *Phys. Rev. X* **10**, 021067 (2020).
- [12] M. Cerezo, A. Sone, T. Volkoff, L. Cincio, and P. J. Coles, Cost function dependent barren plateaus in shallow parametrized quantum circuits, *Nat. Commun.* **12**, 1791 (2021).
- [13] S. Endo, Z. Cai, S. C. Benjamin, and X. Yuan, Hybrid quantum-classical algorithms and quantum error mitigation, *J. Phys. Soc. Jpn.* **90**, 032001 (2021).
- [14] T. Xin, L. Che, C. Xi, A. Singh, X. Nie, J. Li, Y. Dong, and D. Lu, Experimental quantum principal component analysis via parametrized quantum circuits, *Phys. Rev. Lett.* **126**, 110502 (2021).
- [15] Z. Wang, P.-L. Zheng, B. Wu, and Y. Zhang, Quantum dropout: On and over the hardness of quantum approximate optimization algorithm, *Phys. Rev. Res.* **5**, 023171 (2023).
- [16] J. Preskill, Quantum computing in the NISQ era and beyond, *Quantum* **2**, 79 (2018).
- [17] K. Bharti, A. Cervera-Lierta, T. H. Kyaw, T. Haug, S. Alperin-Lea, A. Anand, M. Degroote, H. Heimonen, J. S. Kottmann, T. Menke, W.-K. Mok, S. Sim, L.-C. Kwek, and A. Aspuru-Guzik, Noisy intermediate-scale quantum algorithms, *Rev. Mod. Phys.* **94**, 015004 (2022).
- [18] Y. Cao, J. Romero, J. P. Olson, M. Degroote, P. D. Johnson, M. Kieferová, I. D. Kivlichan, T. Menke, B. Peropadre, N. P. D. Sawaya, S. Sim, L. Veis, and A. Aspuru-Guzik, Quantum chemistry in the age of quantum computing, *Chem. Rev.* **119**, 10856 (2019).
- [19] E. Gil-Fuster, J. Eisert, and C. Bravo-Prieto, Understanding quantum machine learning also requires rethinking generalization, [arXiv:2306.13461](https://arxiv.org/abs/2306.13461).
- [20] B. Bollig and I. Wegener, Improving the variable ordering of obdds is NP-complete, *IEEE Trans. Comput.* **45**, 993 (1996).
- [21] V. Kolmogorov and R. Zabin, What energy functions can be minimized via graph cuts? *IEEE Trans. Pattern Anal. Mach. Intell.* **26**, 147 (2004).

- [22] C. A. Tovey, A simplified NP-complete satisfiability problem, *Discrete Appl. Math.* **8**, 85 (1984).
- [23] S. Sakai, M. Togasaki, and K. Yamazaki, A note on greedy algorithms for the maximum weighted independent set problem, *Discrete Appl. Math.* **126**, 313 (2003).
- [24] Y. Hu, Z. Zhang, and B. Wu, Quantum algorithm for a set of quantum 2SAT problems, *Chin. Phys. B* **30**, 020308 (2021).
- [25] H. Yu, F. Wilczek, and B. Wu, Quantum algorithm for approximating maximum independent sets, *Chin. Phys. Lett.* **38**, 030304 (2021).
- [26] C. A. Trugenberger, Probabilistic quantum memories, *Phys. Rev. Lett.* **87**, 067901 (2001).
- [27] C. Ahn, H. M. Wiseman, and G. J. Milburn, Quantum error correction for continuously detected errors, *Phys. Rev. A* **67**, 052310 (2003).
- [28] W. P. Livingston, M. S. Blok, E. Flurin, J. Dressel, A. N. Jordan, and I. Siddiqi, Experimental demonstration of continuous quantum error correction, *Nat. Commun.* **13**, 2307 (2022).
- [29] A. G. Fowler, M. Mariantoni, J. M. Martinis, and A. N. Cleland, Surface codes: Towards practical large-scale quantum computation, *Phys. Rev. A* **86**, 032324 (2012).
- [30] D. Bluvstein, S. J. Evered, A. A. Geim, S. H. Li, H. Zhou, T. Manovitz, S. Ebadi, M. Cain, M. Kalinowski, D. Hangleiter *et al.*, Logical quantum processor based on reconfigurable atom arrays, *Nature (London)* **626**, 58 (2024).
- [31] A. Matthies, M. Rudner, A. Rosch, and E. Berg, Programmable adiabatic demagnetization for systems with trivial and topological excitations, [arXiv:2210.17256](https://arxiv.org/abs/2210.17256).
- [32] N. A. Rodríguez-Briones and R. Laflamme, Achievable polarization for heat-bath algorithmic cooling, *Phys. Rev. Lett.* **116**, 170501 (2016).
- [33] S. Zaiser, C. T. Cheung, S. Yang, D. B. R. Dasari, S. Raesi, and J. Wrachtrup, Cyclic cooling of quantum systems at the saturation limit, *npj Quantum Inf.* **7**, 92 (2021).
- [34] J. Majer, J. M. Chow, J. M. Gambetta, J. Koch, B. R. Johnson, J. A. Schreier, L. Frunzio, D. I. Schuster, A. A. Houck, A. Wallraff, A. Blais, M. H. Devoret, S. M. Girvin, and R. J. Schoelkopf, Coupling superconducting qubits via a cavity bus, *Nature (London)* **449**, 443 (2007).
- [35] A. Blais, J. Gambetta, A. Wallraff, D. I. Schuster, S. M. Girvin, M. H. Devoret, and R. J. Schoelkopf, Quantum-information processing with circuit quantum electrodynamics, *Phys. Rev. A* **75**, 032329 (2007).
- [36] A. Blais, A. L. Grimsmo, S. M. Girvin, and A. Wallraff, Circuit quantum electrodynamics, *Rev. Mod. Phys.* **93**, 025005 (2021).
- [37] G. Kurizki, P. Bertet, Y. Kubo, K. Mølmer, D. Petrosyan, P. Rabl, and J. Schmiedmayer, Quantum technologies with hybrid systems, *Proc. Natl. Acad. Sci. USA* **112**, 3866 (2015).
- [38] M. Aspelmeyer, T. J. Kippenberg, and F. Marquardt, Cavity optomechanics, *Rev. Mod. Phys.* **86**, 1391 (2014).
- [39] A. N. Cleland and M. R. Geller, Superconducting qubit storage and entanglement with nanomechanical resonators, *Phys. Rev. Lett.* **93**, 070501 (2004).
- [40] M. C. Collodo, J. Herrmann, N. Lacroix, C. K. Andersen, A. Remm, S. Lazar, J.-C. Besse, T. Walter, A. Wallraff, and C. Eichler, Implementation of conditional phase gates based on tunable ZZ interactions, *Phys. Rev. Lett.* **125**, 240502 (2020).
- [41] A. Lucas, Ising formulations of many NP problems, *Front. Phys.* **2**, 1 (2014).
- [42] P. Zhao, P. Xu, D. Lan, J. Chu, X. Tan, H. Yu, and Y. Yu, High-contrast ZZ interaction using superconducting qubits with opposite-sign anharmonicity, *Phys. Rev. Lett.* **125**, 200503 (2020).
- [43] M. Gong, S. Wang, C. Zha, M.-C. Chen, H.-L. Huang, Y. Wu, Q. Zhu, Y. Zhao, S. Li, S. Guo, H. Qian, Y. Ye, F. Chen, C. Ying, J. Yu, D. Fan, D. Wu, H. Su, H. Deng, H. Rong *et al.*, Quantum walks on a programmable two-dimensional 62-qubit superconducting processor, *Science* **372**, 948 (2021).
- [44] A. D. King, S. Suzuki, J. Raymond, A. Zucca, T. Lanting, F. Altomare, A. J. Berkley, S. Ejtemaee, E. Hoskinson, S. Huang, E. Ladizinsky, A. J. R. MacDonald, G. Marsden, T. Oh, G. Poulin-Lamarre, M. Reis, C. Rich, Y. Sato, J. D. Whittaker, J. Yao *et al.*, Coherent quantum annealing in a programmable 2000 qubit Ising chain, *Nat. Phys.* **18**, 1324 (2022).
- [45] M. F. Gely, A. Parra-Rodríguez, D. Bothner, Y. M. Blanter, S. J. Bosman, E. Solano, and G. A. Steele, Convergence of the multi-mode quantum Rabi model of circuit quantum electrodynamics, *Phys. Rev. B* **95**, 245115 (2017).
- [46] M. Malekakhlagh, A. Petrescu, and H. E. Türeci, Cutoff-free circuit quantum electrodynamics, *Phys. Rev. Lett.* **119**, 073601 (2017).
- [47] T. Miyanaga, A. Tomonaga, H. Ito, H. Mukai, and J.S. Tsai, Ultrastrong tunable coupler between superconducting LC resonators, *Phys. Rev. Appl.* **16**, 064041 (2021).
- [48] M. V. P. Altoé, A. Banerjee, C. Berk, A. Hajr, A. Schwartzberg, C. Song, M. Alghadeer, S. Aloni, M. J. Elowson, J. M. Kreikebaum, E. K. Wong, S. M. Griffin, S. Rao, A. Weber-Bargioni, A. M. Minor, D. I. Santiago, S. Cabrini, I. Siddiqi, and D. F. Ogletree, Localization and mitigation of loss in niobium superconducting circuits, *PRX Quantum* **3**, 020312 (2022).
- [49] R. Kuzmin, N. Mehta, N. Grabon, R. Mencia, and V. E. Manucharyan, Superstrong coupling in circuit quantum electrodynamics, *npj Quantum Inf.* **5**, 20 (2019).
- [50] P. Talkner and P. Hänggi, *Colloquium: Statistical mechanics and thermodynamics at strong coupling: Quantum and classical*, *Rev. Mod. Phys.* **92**, 041002 (2020).
- [51] J. Liu, K. A. Jung, and D. Segal, Periodically driven quantum thermal machines from warming up to limit cycle, *Phys. Rev. Lett.* **127**, 200602 (2021).
- [52] M. Um, J. Zhang, D. Lv, Y. Lu, S. An, J.-N. Zhang, H. Nha, M. S. Kim, and K. Kim, Phonon arithmetic in a trapped ion system, *Nat. Commun.* **7**, 11410 (2016).
- [53] D. I. Schuster, A. A. Houck, J. A. Schreier, A. Wallraff, J. M. Gambetta, A. Blais, L. Frunzio, J. Majer, B. Johnson, M. H. Devoret, S. M. Girvin, and R. J. Schoelkopf, Resolving photon number states in a superconducting circuit, *Nature (London)* **445**, 515 (2007).
- [54] A. Caldeira and A. Leggett, Path integral approach to quantum Brownian motion, *Physica A* **121**, 587 (1983).
- [55] A. Polkovnikov, Phase space representation of quantum dynamics, *Ann. Phys. (NY)* **325**, 1790 (2010).
- [56] T. L. Curtright and C. K. Zachos, Quantum mechanics in phase space, *Asia Pacific Phys. Newslett.* **01**, 37 (2012).
- [57] Z. Wang, J. Feng, and B. Wu, Microscope for quantum dynamics with Planck cell resolution, *Phys. Rev. Res.* **3**, 033239 (2021).
- [58] Q. Zhang and B. Wu, General approach to quantum-classical hybrid systems and geometric forces, *Phys. Rev. Lett.* **97**, 190401 (2006).

- [59] A. M. Childs and J. Goldstone, Spatial search by quantum walk, *Phys. Rev. A* **70**, 022314 (2004).
- [60] A. M. Childs, Universal computation by quantum walk, *Phys. Rev. Lett.* **102**, 180501 (2009).
- [61] S. E. Venegas-Andraca, Quantum walks: A comprehensive review, *Quantum Inf. Process.* **11**, 1015 (2012).
- [62] Y. Liu, W. J. Su, and T. Li, On quantum speedups for nonconvex optimization via quantum tunneling walks, *Quantum* **7**, 1030 (2023).
- [63] J. Casanova, G. Romero, I. Lizuain, J. J. García-Ripoll, and E. Solano, Deep strong coupling regime of the Jaynes-Cummings model, *Phys. Rev. Lett.* **105**, 263603 (2010).
- [64] F. Casas, A. Murua, and M. Nadinic, Efficient computation of the Zassenhaus formula, *Comput. Phys. Commun.* **183**, 2386 (2012).
- [65] J. Kempe, Quantum random walks: An introductory overview, *Contemp. Phys.* **44**, 307 (2003).
- [66] I. Carneiro, M. Loo, X. Xu, M. Girerd, V. Kendon, and P. L. Knight, Entanglement in coined quantum walks on regular graphs, *New J. Phys.* **7**, 156 (2005).
- [67] N. Shenvi, J. Kempe, and K. Birgitta Whaley, Quantum random-walk search algorithm, *Phys. Rev. A* **67**, 052307 (2003).
- [68] K. Y. Tan, M. Partanen, R. E. Lake, J. Govenius, S. Masuda, and M. Möttönen, Quantum-circuit refrigerator, *Nat. Commun.* **8**, 15189 (2017).
- [69] M. Silveri, H. Grabert, S. Masuda, K. Y. Tan, and M. Möttönen, Theory of quantum-circuit refrigeration by photon-assisted electron tunneling, *Phys. Rev. B* **96**, 094524 (2017).
- [70] H. Hsu, M. Silveri, A. Gunyhó, J. Goetz, G. Catelani, and M. Möttönen, Tunable refrigerator for nonlinear quantum electric circuits, *Phys. Rev. B* **101**, 235422 (2020).
- [71] M. Raghunandan, F. Wolf, C. Ospelkaus, P. O. Schmidt, and H. Weimer, Initialization of quantum simulators by sympathetic cooling, *Sci. Adv.* **6**, eaaw9268 (2020).
- [72] S. Polla, Y. Herasymenko, and T. E. O'Brien, Quantum digital cooling, *Phys. Rev. A* **104**, 012414 (2021).
- [73] P. A. Camati, J. F. G. Santos, and R. M. Serra, Employing non-Markovian effects to improve the performance of a quantum Otto refrigerator, *Phys. Rev. A* **102**, 012217 (2020).
- [74] Q. Zhang, Z.-X. Man, and Y.-J. Xia, Non-Markovianity and the Landauer principle in composite thermal environments, *Phys. Rev. A* **103**, 032201 (2021).
- [75] R. Harris, T. Lanting, A. J. Berkley, J. Johansson, M. W. Johnson, P. Bunyk, E. Ladizinsky, N. Ladizinsky, T. Oh, and S. Han, Compound Josephson-junction coupler for flux qubits with minimal crosstalk, *Phys. Rev. B* **80**, 052506 (2009).
- [76] X. Dai, D. M. Tennant, R. Trappen, A. J. Martinez, D. Melanson, M. A. Yurtalan, Y. Tang, S. Novikov, J. A. Grover, S. M. Disseler, J. I. Basham, R. Das, D. K. Kim, A. J. Melville, B. M. Niedzielski, S. J. Weber, J. L. Yoder, D. A. Lidar, and A. Lupascu, Calibration of flux crosstalk in large-scale flux-tunable superconducting quantum circuits, *PRX Quantum* **2**, 040313 (2021).
- [77] A. M. van den Brink, A. J. Berkley, and M. Yalowsky, Mediated tunable coupling of flux qubits, *New J. Phys.* **7**, 230 (2005).
- [78] X. Qiu, P. Zoller, and X. Li, Programmable quantum annealing architectures with Ising quantum wires, *PRX Quantum* **1**, 020311 (2020).
- [79] Y. P. Zhong, H. S. Chang, K. J. Satzinger, M. H. Chou, A. Bienfait, C. R. Conner, E. Dumur, J. Grebel, G. A. Peairs, R. G. Povey, D. I. Schuster, and A. N. Cleland, Violating Bell's inequality with remotely connected superconducting qubits, *Nat. Phys.* **15**, 741 (2019).
- [80] P. Zhao, K. Linghu, Z. Li, P. Xu, R. Wang, G. Xue, Y. Jin, and H. Yu, Quantum crosstalk analysis for simultaneous gate operations on superconducting qubits, *PRX Quantum* **3**, 020301 (2022).
- [81] B. Kannan, M. J. Ruckriegel, D. L. Campbell, A. Frisk Kockum, J. Braumüller, D. K. Kim, M. Kjaergaard, P. Krantz, A. Melville, B. M. Niedzielski, A. Vepsäläinen, R. Winik, J. L. Yoder, F. Nori, T. P. Orlando, S. Gustavsson, and W. D. Oliver, Waveguide quantum electrodynamics with superconducting artificial giant atoms, *Nature (London)* **583**, 775 (2020).
- [82] Y. Zhong, H.-S. Chang, A. Bienfait, E. Dumur, M.-H. Chou, C. R. Conner, J. Grebel, R. G. Povey, H. Yan, D. I. Schuster, and A. N. Cleland, Deterministic multi-qubit entanglement in a quantum network, *Nature (London)* **590**, 571 (2021).
- [83] A. Schreiber, K. N. Cassemiro, V. Potoček, A. Gábris, I. Jex, and C. Silberhorn, Decoherence and disorder in quantum walks: From ballistic spread to localization, *Phys. Rev. Lett.* **106**, 180403 (2011).
- [84] D. A. Abanin, E. Altman, I. Bloch, and M. Serbyn, *Colloquium: Many-body localization, thermalization, and entanglement*, *Rev. Mod. Phys.* **91**, 021001 (2019).
- [85] A. C. Potter, R. Vasseur, and S. A. Parameswaran, Universal properties of many-body delocalization transitions, *Phys. Rev. X* **5**, 031033 (2015).
- [86] M. Serbyn, Z. Papić, and D. A. Abanin, Criterion for many-body localization-delocalization phase transition, *Phys. Rev. X* **5**, 041047 (2015).
- [87] B. Zeng, X. Chen, D.-L. Zhou, and X.-G. Wen, *Quantum Information Meets Quantum Matter* (Springer, New York, 2019).
- [88] D. J. Luitz, N. Laflorencie, and F. Alet, Many-body localization edge in the random-field Heisenberg chain, *Phys. Rev. B* **91**, 081103(R) (2015).
- [89] R. Harris, J. Johansson, A. J. Berkley, M. W. Johnson, T. Lanting, S. Han, P. Bunyk, E. Ladizinsky, T. Oh, I. Perminov, E. Tolkacheva, S. Uchaikin, E. M. Chapple, C. Enderud, C. Rich, M. Thom, J. Wang, B. Wilson, and G. Rose, Experimental demonstration of a robust and scalable flux qubit, *Phys. Rev. B* **81**, 134510 (2010).
- [90] M. Xiao and H. Nagamochi, Exact algorithms for maximum independent set, *Inform. Comput.* **255**, 126 (2017).
- [91] C.-F. Chen, H.-Y. Huang, J. Preskill, and L. Zhou, Local minima in quantum systems, [arXiv:2309.16596](https://arxiv.org/abs/2309.16596).
- [92] M. Orszag and J. Retamal, *Modern Challenges in Quantum Optics* (Springer, Berlin, 2001).
- [93] X. Li, Y. Zhou, and H. Zhang, Manipulating atom-cavity interactions with configurable atomic chains, [arXiv:2308.07908](https://arxiv.org/abs/2308.07908).
- [94] V. Kendon and B. Tregenna, Decoherence can be useful in quantum walks, *Phys. Rev. A* **67**, 042315 (2003).